RSC Advances

ROYAL SOCIETY
OF CHEMISTRY

www.rsc.org/advances

Journal Name

ARTICLE

Carbonate-assisted hydrothermal synthesis of porous, hierarchical CuO microspheres and CuO/GO for high-performance lithium-ion battery anodes

Lin Shi, Xinxin Fu, Chenyao Fan, Siqi Yu, Guodong Qian and Zhiyu Wang*

Porous, hierarchical CuO microspheres (MSs) have been successfully synthesized through a facile, surfactant-free carbonate-assisted hydrothermal method. A growth mechanism based on self-aggregate and decomposition of precursor $Cu_2(OH)_2CO_3$ nanoparticles and Ostwald ripening under hydrothermal condition is proposed to explain the formation of CuO MSs. Then the CuO MSs are encapsulated with GO through engineering the ionic strength in solution and applied as anode materials for lithium ion batteries, which demonstrates that CuO/GO exhibits significant improvements over the bare CuO MSs. It can deliver a high reversible capacity of 500 mAh g^{-1} after 500 cycles, with 80 % capacity retention of the second reversible capacity (625.8 mAh g^{-1}) at a current density of 0.5 C. This is much higher than 233.5 mAh g^{-1} of the bare CuO MSs at the same rate. Such significant enhanced electrochemical performance of CuO/GO hybrid can be contributed to the synergistic effect of successful integration of the CuO MSs with the high conductive and flexible GO sheets. This study demonstrates that facile structural tuning of metal oxide in combination with advantageous carbon materials is a promising way to fabricate anodes for high-performance lithium-ion batteries.

1. Introduction

As a very promising energy storage device, lithium-ion batteries (LIBs) have become the focus of energy storage system research for the applications in modern portable electronics, hybrid electric vehicles and sensor networks. [1-5] Generrally, a LIB device consists of four key components, namely the anode, electrolyte, separator and cathode. It is based on the shuttling of Li-ions between the anode and the cathode that makes LIBs function as a power source. Hence, the electrode materials play a vital role in the electrochemical lithium storage of LIBs, and have great influence on battery performance such as charge/discharge capacity, cycle stability and rate performance.[6-10] Therefore, facile and efficient synthesis of electrodes with excellent electrochemical performance for LIBs is of highly significance for future energy storage applications.

Recently, Poizot *et al.* demonstrated that nano-sized transition metal oxides that served as new electrode materials based on conversion mechanism exhibited promising electrochemical performance in terms of specific capacities and capacity retention.[11] Thus, transition metal oxides such as

Fe_3O_4 [12-13], Co_3O_4 [14-15], Mn_3O_4 [16-17] and CuO [18-20] have attracted much attention as potential anodes for next generation LIBs owing to their much higher theoretical capacities compared with that of commercial graphite anode (372 mAh g^{-1}). Especially, copper oxide (CuO) as a p-type semiconductor has been widely investigated as an anode due to its high theoretical capacity (674 mAh g^{-1}), natural abundance, environment benignity and easy preparation. Unfortunately, its practical application in LIBs is still hindered by its intrinsically low conductivity which is not favorable for charge transport and its drastic volume variation during repeated Li^+ intercalation and deintercalation which lead to electrode pulverization and rapid capacity fading. Therefore, it is still a big challenge to enhance the electrochemical performance of CuO in LIBs.

To resolve the above issues, many approaches have been attempted to improve the electrochemical properties of CuO-based anode electrodes including micro/nanostructured design and controlled synthesis. This strategy has promoted the development of various CuO structures such as porous, hollow, nanocrystalline-assembled and hierarchical architectures for LIBs with enhanced electrochemical performance in recent years. For example, hierarchical self-assembly of microscale cog-like CuO superstructures on Cu foil were prepared by Zhang *et al.* through a novel microemulsion-mediated method, which exhibited excellent rate performance that a discharge capacity of 583 mAh g^{-1} was remained even at a rate of 2400 mA g^{-1}. [18] What's more, Deng *et al.* [21] successfully synthesized high-order 3D meso-oblate spheroids of CuO nanoparticle aggregate with size-tunable building nanounits, and then tested

State Key Laboratory of Silicon Materials, School of Materials Science and Engineering, Zhejiang University, Hangzhou 310027, China.
E-mail: wangzhiyu@zju.edu.cn
Fax: +86-0571-87952539; Tel: +86-0571-87952539

RSC Advances Accepted Manuscript

for reversible lithium ion storage with a reversible capacity of 600 mAh g^{-1} for 20 cycles at a rate of 100 mAh g^{-1}. In our preliminary work, porous CuO nanoleaves and nanocrystlline-assembled CuO nanorods were obtained through changing the drying medium of Cu(OH)$_2$ nanorods precursors, and both novel nanostructured CuO displayed high capacity and excellent cycling stability. [22] Complicated synthesis process, post heat treatment and surfactant-assistant make these methods far from industrial-scale applications. Thus, the development of simple, facile, surfactant-free and scalable methodologies to fabricate novel nanostructured CuO remains a challenge. What's more, though those novel CuO structures demonstrate better electrochemical performance than bulk powder electrodes, low electric conductivity is still a barrier for practical application. Therefore, there is another effective way to fabricate promising anode materials for LIBs by introducing a highly conductive layer. It is worth noting that attempts have also been made to improve the performance of CuO-based electrodes by coating with carbon or polymer materials, such as carbon nanotube [23-25], graphene [26-27], reduced graphene oxide (rGO) [28], polypyrrole [29], PEDOTs. However, there are few reports on integrating facile synthesized porous hierarchical CuO microstructures with super properties of GO to enhance the performance of CuO.

Herein, we have developed an environmentally benign, template-free, and scalable carbonate-assisted hydrothermal method for the synthesis of porous hierarchical CuO microspheres constructed by CuO nanorods as building units. Then porous CuO MSs were encapsulated with GO through a method of engineering the ionic strength in solution proposed by Rong *et al.*. [30] The structures of the products are comprehensively characterized and their electrochemical properties are investigated in detail. By comparing with bare CuO electrode, the CuO/GO hybrid anode delivers enhanced cycling and rate performance. Our result demonstrates a facile method to synthesis CuO hierarchical microspheres and this strategy combining synthesis of special MO structures with carbon-coating is very effective for fabricating potential anode materials for high-performance LIBs.

2. Experimental section

2.1 Materials

Copper sulfate pentahydrate (CuSO$_4$·5H$_2$O), sodium carbonate (Na$_2$CO$_3$) and sodium chloride (NaCl) were all purchased from Sinopharm Chemical Reagent Co., Ltd., Shanghai, China. Graphene oxide (GO) solution (2 g L^{-1}) was obtained from Institute of Coal Chemistry, Chinese Academy of Sciences. All chemicals were of analytical grade and used as received without further purification.

2.2 Synthesis of CuO microspheres (CuO MSs)

In a typical synthesis, 4 mmol CuSO$_4$·5H$_2$O was dissolved in 50 mL of deionized water. Then 20 mL of 0.6 M Na$_2$CO$_3$ aqueous solution was added in and stirred at room temperature for 30 min. Subsequently, the mixture was transferred into a

100 mL Teflon-lined stainless steel autoclave and heated to 200 ^{o}C for 4 h, which was allowed to cool to room temperature naturally. The black precipitate was separated by centrifugation, washed with water and ethanol for several times, and dried at 60 ^{o}C for 12 h.

2.3 Synthesis of CuO/GO composite

To synthesis CuO/GO composite, a proposed generic strategy based on solution ionic strength to coat GO on various functional particles was employed. [30] First, 160 mg CuO (CuO-MSs) was dispersed in 40 mL of 1 M NaCl aqueous solution and 10 mL of GO aqueous solution was mixed with 30 mL of 1 M NaCl aqueous solution through ultrasonic treatment for 10 min, respectively. Then, the two suspensions were mixed together and stirred for 1 h. The precipitate was collected and washed with water and ethanol using centrifugation, and dried at 60 ^{o}C for 12 h. The product was denoted as CuO/GO composite.

2.4 Material characterization

The XRD pattern was conducted on a powder X-Ray diffraction (XRD; Philips, PW1050, Cu Kα radiation, λ = 1.5406 Å). Morphology and structure of samples were analyzed using transmission electron microscopy (TEM; JEOL, JEM-1230) operating at accelerating voltages of 80 kV and scanning electron microscopy (SEM; HITACHI-4800). The structure and selected area electron diffraction were measured by High-resolution TEM (HRTEM; TECNAI G2 F20) at 200 kV. Fourier transform infrared spetra (FT-IR) were recorded on a Bruker Vector 22 FT-IR spectrometer (FT-IR, Germany) using KBr pellets. Nitrogen adsorption and desorption were conducted employing Tristar II 3020 surface and porosity analyzer at 77 K. The surface area was calculated using the Brunauer-Emmett-Teller (BET) equation. The pore size distribution was estimated from the desorption branch of the isotherm curves using the Barrett-Joyner-Halenda (BJH) model. Thermogravimetric analysis (TGA) was performed on a CHNS/O analyzer (PE 2400II, PerkinElmer, America) in air atmosphere from room temperature to 800 ^{o}C with a heating rate of 10 ^{o}C min^{-1}.

2.5 Electrochemical Measurement

The electrochemical characterization was investigated with CR2025-type coin cells containing the CuO working electrode and metallic lithium foil as the combined reference and counter electrodes. The working electrodes were prepared by using CuO or CuO/GO as the active material, acetylene black and polyvinylidene fluoride (PVDF) binder in a weight ratio of 80: 10: 10, dispersed in N-methyl-2-pyrrolidinone. The slurry was uniformly coated on copper foils, and dried in a vacuum oven at 120 °C for 12 h to remove the solvent before pressing. Celgard 2400 polypropylene membrane was used as a separator and the electrolyte consisted of 1 M LiPF$_6$ in a mixture of 1:1:1 (v: v: v) ethylene carbonate (EC)-dimethyl carbonate (DMC)-diethyl carbonate (DEC). The cells were assembled in an argon-filled glove box. Galvanostatic discharge-charge cycles were tested by LAND CT2001A battery test system (Wuhan Land

Electronic Co., China) at current density based on the weight of the active material between 3V and 0.001 V *vs.* Li/Li$^+$ at room temperature. Cyclic voltammetry (CV) measurements were conducted on an Arbin electrochemical workstation at a scan rate of 0.1 mV s^{-1} from 0 V to 3.0 V (*vs.* Li/Li$^+$). Electrochemical impedance spectra (EIS) were conducted on a CHI 660D electrochemical workstation (Chenhua Shanghai, China) in the frequency range from 100 kHz to 10 mHz.

3. Results and discussion

The composition and phase purity of the as-synthesized samples (GO, CuO MSs and CuO/GO) were determined by XRD as shown in Fig. 1. All the diffraction peaks of CuO MSs and CuO/GO samples can be indexed to the monoclinic symmetry of CuO (space group C2/c, JCPDS file no. 05-0661). No other diffraction peaks are observed, indicating high purity of the as-prepared samples. Moreover, the characteristic reflection peak of GO centers at 2θ=10.7^o, corresponding to an interplanar spacing of 0.84 nm which is not clearly observed for the CuO/GO hybrid sample due to its relatively low content and weak peak intensity compared to that of CuO.

Fourier-transform infrared (FT-IR) is also taken in order to provide evidence for the successfully introduction of GO into the composite. Fig. 2 shows the FT-IR spectra of GO, CuO MSs and CuO/GO composites. The broad absorption bands at about 3423 and 1623 cm^{-1} are assigned to the hydroxyl groups. The absorption band at 1053 cm^{-1} can be assigned to the stretching vibration of C-O. Furthermore, the absorption band at 520 cm^{-1} is attributed to the vibration of Cu-O bond.[31] Except for the absorption band assigned to the Cu-O bond, FT-IR spectra from the CuO/GO hybrid exhibits exactly the same peak positions as that of GO, confirming the existence of GO in the CuO/GO hybrid and no chemical reactions between CuO and GO in the coating process.

The morphologies and structures of the CuO MSs and CuO/GO were characterized by SEM and TEM. As shown in Fig. 3, the hydrothermal synthesized CuO are microspheres with the diameter of 1.5- 2.0 μm. It is clearly observed in Fig. 3b that the hierarchical CuO MSs structures are consisted of
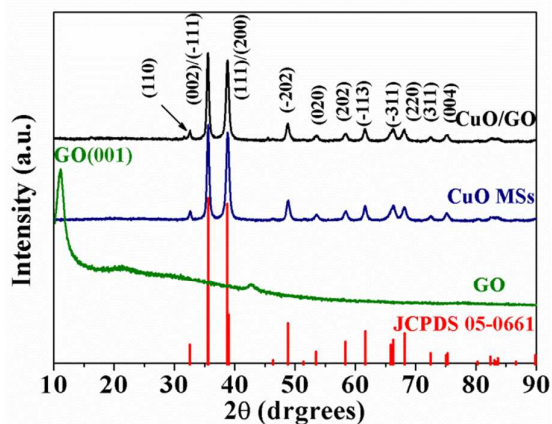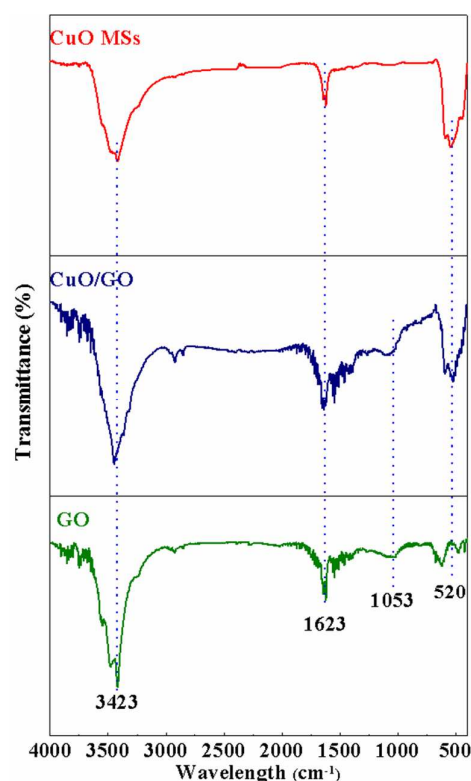

Fig. 2 FT-IR spectra of GO, CuO MSs and CuO/GO composite.

nanorods. Furthermore, the high-magnification TEM image (Fig. 3d) discloses that the CuO MS are porous, and the formation of the pores can be contributed to the self-aggregation of CuO nanoparticles and the Oswald-effect, which will be elucidated in detail later. The porous feature of the as-prepared CuO MSs was determined by nitrogen adsorption-
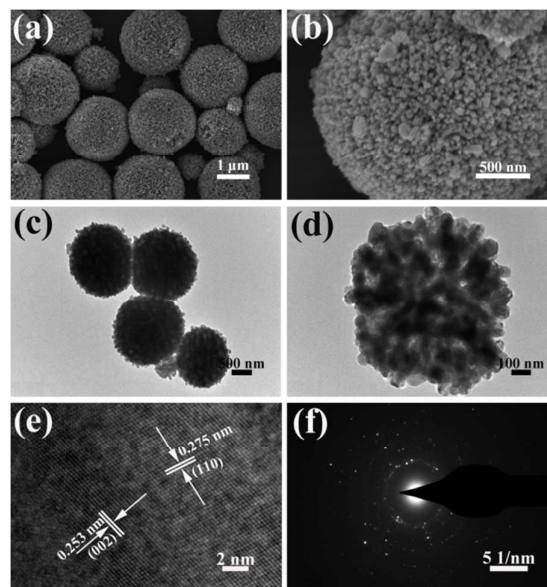

Fig. 3 SEM and TEM images of CuO MSs: (a),(c) low-magnification SEM and TEM, respectively; (b), (d) high-magnification SEM and TEM, respectively; (e) HRTEM image of the nanorods. (f) SAED image of CuO MSs.

Fig. 1 X-Ray diffraction patterns of GO, CuO MSs and CuO/GO composite.

desorption measurements (Fig. S1a†), which delivers that the CuO MSs give a high specific surface area of 18 m^2g^{-1} and total pore volume of 0.166 m^3g^{-1}. The measured planar spacing of 0.275nm and 0.253 nm could be identified in the HRTEM image of CuO (Fig. 3e), which are in good agreement with the (110) and (002) crystalline plane of the monoclinic CuO, respectively. Several concentric diffraction rings in selected area electron diffraction (SAED) pattern (Fig. 3f) indicates the polycrystalline nature of the microspheres.

After introduction of GO, the CuO/GO composites basically maintain the spherical morphology as shown in Fig. 4a and b, and the majority of CuO MSs are wrapped by GO sheets. What's more, a typical single CuO MS is encapsulated well by GO sheets in TEM image (Fig. 4c), which further confirms the effective coating method developed by Rong *et al* [30]. Similarly, an interplanar spacing of 0.275 nm can be identified in the HRTEM image of CuO/GO (Fig. 4d), which agrees well with the (110) crystalline plane of the CuO in Fig.1. And some folds typically for GO are found in GO sheets (labelled in Fig. 4d). [28] The CuO/GO composites exhibit a much higher specific surface area of 31m^2g^{-1} and little lower total pore volume of 0.132 m^3g^{-1} (Fig. S1b†) than that of bare CuO MSs owing to the incorporation of GO which has a high surface area and encapsulates on the surface of CuO. To determinate the content of GO in the hybrid material, we conducted TG analysis from room temperature to 800 °C under air (Fig. S2†). The weight loss is about 12.5 % from 100 °C to 400 °C, due to the elimination of oxygen-containing functional groups and combustion of carbon-carbon linkage in GO sheets.[27] Thus, the content of GO in the composite is about 12.5 %, which is consistent with the experimental conditions.

To understand the detailed growth process of CuO MSs, time-dependent and temperature- dependent experiments were carrying out by keeping all other reaction parameters unchanged. The SEM images of the corresponding intermediates are shown in Fig. 6 and Fig. S3-4†. After stirring at room temperature for 0.5 h, blue irregular $Cu_2(OH)_2CO_3$ nanoparticles (Fig. 5a) are obtained. Only one broad diffraction peak can be seen from the XRD pattern of the precursor (Fig. S6a†), indicating the $Cu_2(OH)_2CO_3$ nanoparticles are amorphous. Furthermore, Fig. S6b† shows the FT-IR spectra of the precursor, the deformation band of the OH group at 1384

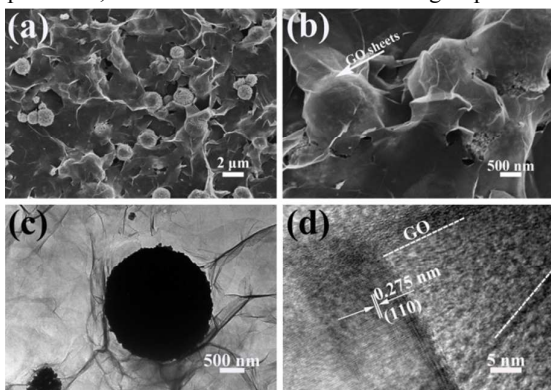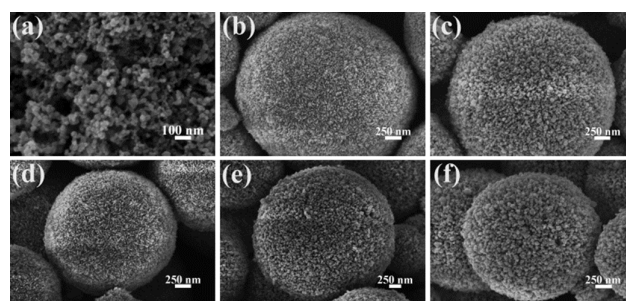**Fig. 4** (a), (b) SEM images; (c) TEM image; (d) HRTEM image of CuO/GO hybrid.

Fig.5 SEM images of CuO synthesized under different reaction conditions: (a)25 °C-0.5 h, (b) 120 °C-4h, (c) 160 °C-4 h, (d) 200 °C-0.5 h, (e) 200 °C-1 h and (f) 200 °C-2 h.

cm^{-1}, the stretching vibration band of C=O group at 1474 cm^{-1} and 837 cm^{-1}, respectively, confirm that the amorphous precursor is $Cu_2(OH)_2CO_3$; when compared with the FT-IR spectra of CuO MSs, this result further demonstrates the phase-purity of hydrothermal synthesized CuO MSs. In contrast, after hydrothermal treatment CuO MSs composed of nanorods are successfully synthesized, and some differences of the nanorods can be observed from the high-magnification SEM images. The growth of the nanorods can be clearly displayed when the reaction duration at 200 °C is extended from 0.5 h to 2 h (Fig. 5d-f, Fig. S4-5†), or the reaction temperature is increased from 120 °C to 160 °C (Fig. 5b, c). For the sample obtained at 200 °C for 4 hours, larger nanorods endow the CuO MS with larger space which is beneficial for improving its electrochemical performance. Thus, both temperature and time paly a vital role in controlling the morphology and structure of products from the carbonate-assisted hydrothermal reaction. We further study the effect of the couterions on the formation of CuO MSs. Three different copper salts $CuCl_2$, $Cu(NO_3)_2$ and $Cu(CH_3COO)_2$ with different counterions were chosen, and all other experimental parameters were kept constant. No matter of which copper salt is chosen, hierarchical CuO MSs are formed, as shown in Fig. S7†. From these experiments, it can be concluded that the counterion in the copper salt has no influence on the morphology and structure of the CuO, indicating this hydrothermal method is more facile.

The synthesis process and its corresponding structural variation of CuO/GO composites are schematically illustrated in Fig. 6. Briefly, there are two steps in synthesizing CuO/GO hybrid. Firstly, bare porous CuO MSs are obtained from the self-aggregation and decomposition of precursor $Cu_2(OH)_2CO_3$ nanoparticles via a carbonate-assisted hydrothermal method. The nanoparticles which initially serve as building blocks of MSs are synthesized in large scale by a precipitation between $CuSO_4$ and Na_2CO_3 at room temperature. Hence, at appropriate hydrothermal condition, many CuO nanocrystals are produced due to the decomposition of $Cu_2(OH)_2CO_3$ precursors according to the reaction: $Cu_2(OH)_2CO_3 \rightarrow 2CuO+H_2O+CO_2$. Furthermore, owing to high surface energy the nanoparticles start to self-aggregate to form spheres. With continuous reaction, the CuO nanoparticles gradually grow up and convert into CuO nanorods and nanoporous CuO MSs are formed for the Ostwald ripening. Secondly, CuO MSs are successfully wrapped with GO by engineering the ionic strength of NaCl
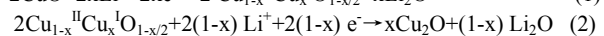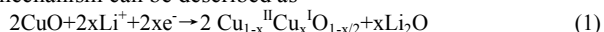
RSC Advances

Fig. 6 Schematic illustration of the synthesis process for CuO MSs and CuO/GO hybrid.

aqueous solution. After dispersing GO in the high concentration ionic solution (NaCl(aq)), the GO will lose electrostatic repulsive and take hours to precipitate out because of their low density. [28] During this process, the introduction of CuO MSs leads to GO coating on their surfaces to minimize the surface energy. Especially, nanoporous CuO MSs are successfully synthesized by a one-pot, surfactant-free carbonate-assisted hydrothermal method, which is based on the precursor $Cu_2(OH)_2CO_3$ instead of the general morphology-controlled precursor $Cu(OH)_2$ for fabrication of CuO nanostructures (cog-like superstructures,[18] nanowires,[26] nanoleaves,[22, 29] nanotubes,[32] *etc.*).

The unique composite microstructures of GO coating porous CuO MSs make them promising anode materials for energy storage application. Therefore, we investigated the electrochemical performance of the CuO/GO hybrid and bare CuO MSs as anode materials for LIBs. The electrochemical behaviour of the synthesized CuO was examined by CV at a scan rate of 0.1 mV s^{-1} in Fig. 7. Three reduction peaks are observed similarly for both as-prepared CuO samples at 0.87 V, 1.18 V and 1.62 V (vs Li$^+$/Li) during the first discharge cycle (Fig. 7a, c), indicating that the introduction of GO has no influence on the redox reaction between CuO and Li. These peaks indicate a multistep electrochemical reaction, including a formation of a solid-solution $Cu^{II}_{1-x}Cu^{I}_{x}O_{1-x/2}$, then transforming into Cu_2O phase, and further decomposition of Cu_2O

into Cu and Li$_2$O. [26, 33-35] During the subsequent charging process, one broad oxidation peak is found at 2.45 V for both CuO samples, which corresponds to the partial oxidization of Cu to Cu_2O and CuO.[36-38] Thus, the electrochemical reaction mechanism can be described as [26, 33]

$$2CuO+2xLi^++2xe^-\rightarrow 2\,Cu^{II}_{1-x}Cu^{I}_{x}O_{1-x/2}+xLi_2O \qquad (1)$$
$$2Cu^{II}_{1-x}Cu^{I}_{x}O_{1-x/2}+2(1-x)\,Li^++2(1-x)\,e^-\rightarrow xCu_2O+(1-x)\,Li_2O \quad (2)$$
$$Cu_2O+2Li^++2e^-\rightarrow 2Cu+Li_2O \qquad (3)$$

In addition, partial irreversible electrolyte decomposition and growth of a solid electrolyte interphase (SEI) layer on the electrode surface also take place.[23,26-28, 39] During subsequent cycles (2nd, third and fifth), all cathodic and anodic peaks of bare CuO MSs and CuO/GO electrodes are reproductive, indicating high reversibility for the redox reaction. Fig. 7b, d reveals the first, second, fifth, 50th, 100th, 150th and 200th charge/discharge voltage profiles of the as-prepared CuO samples at a rate of 0.5 C (1 C= 670 mAh g^{-1}). The multiple plateaus in the discharge curves demonstrate that multiphase transition between CuO and lithium, which is consistent with the CV curves. The initial charge and discharge capacities of the CuO/GO hybrid are found to be 912.8 mAh g^{-1} and 610.5 mAh g^{-1}, which are higher than those of bare CuO MSs (834.3 mAh g^{-1} and 535.4 mAh g^{-1}). The irreversible capacity loss mainly result from the formation of SEI layer, interfacial lithium storage and electrolyte decomposition.[23, 40]
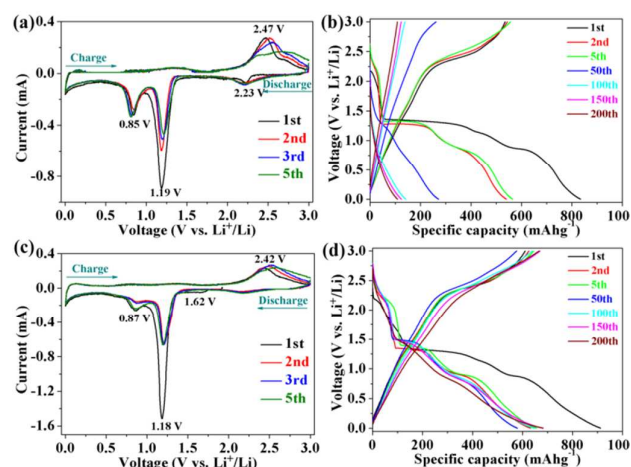
Fig. 7 (a, c) CV curves between 0 and 3 V (*vs.* Li/Li$^+$) at a scan rate of 0.1 mV s^{-1} and (c, d) selected galvanostatic charge-discharge curves between 0.001 and 3 V (*vs.* Li/Li$^+$) at a current density of 0.5 C of (a, b) bare CuO MSs and (c, d) CuO/GO hybrid.

Fig. 8 (a) Cycling performance at a current density of 0.5 C, (b) rate capacity at various current densities and (d) EIS spectra after 20 cycles at 0.1 C of bare CuO MSs and CuO/GO hybrid (the inset is the equivalent circuit used to fit the Nyquist plots).

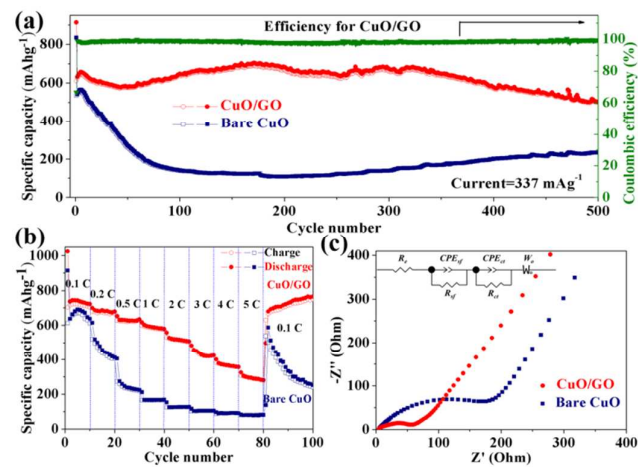Fig. 8a displays the cycling performances of the two CuO electrodes with a current density of 0.5 C for 500 cycles. The CuO/GO hybrid electrode demonstrates much better cycling performance than that of the bare CuO electrode. The CuO/GO hybrid electrode delivers high reversible capacity and the Coulombic efficiency is generally near 98% from the second cycle onwards. Even after 500 cycles, the reversible capacity is still as high as 500.0 mAh g^{-1}, with 80% retention of the second reversible capacity (625.8 mAh g^{-1}). Furthermore, the reversible capacity retains 425.1 mAh g^{-1} even after 960 cycles at 0.5 C (Fig. S7†). This performance is remarkable compared with many works reported previously.[21-23, 25-26] It is worth noting that the capacity of CuO/GO hybrid electrode gradually decreases to 573 mAh g^{-1} in the first 40 cycles owing to the irreversible processes, such as interfacial lithium storage, the formation of SEI layer and the electrolyte decomposition; then capacity slowly increases to 691.0 mAh g^{-1} after 170 cycles which may result from the activation of the porous CuO MSs, because the interiors of the porous CuO MSs are probably not in good contact with the electrolyte and the formation of the SEI layer may need a number of cycles. [39, 41]As the cycle number continues to increase, the reversible capacity maintains stable till 350 cycles and slowly decreases to 500 mAh g^{-1} after 500 cycles. One possible reason for the specific capacity based on the total weight of CuO and GO of the CuO/GO hybrid electrode higher than the theoretical specific capacity of CuO may be due to the formation of gel-like polymer layer on the surface of CuO by electrolyte decomposition as proposed by S. Laruelle *et.al.*[40] (interfacial interaction between the oxide and matrices.) In contrast, the bare CuO exhibits fast capacity decay and low capacity of 233.5 mAh g^{-1} after 500 cycles at the same current rate. Also, the capacity of bare CuO electrode decreases at first and increases later for the same possible reason as discussed above.

Fig. 8b exhibits the rate performance of the two CuO electrodes at different current densities. On the whole, the high-rate performance of the CuO/GO is superior to that of bare CuO. It can be observed that the CuO/GO delivers a discharge capacity of 722.5 mAh g^{-1} at 0.1 C for ten cycles, then this value gradually decreases to 679.0, 634.4, 579.3, 507.1, 423.4, 356.6, 280.9 mAh g^{-1} when the discharge rate is consecutively set at the levels of 0.2 C, 0.5 C, 1 C, 2 C, 3 C, 4 C and 5 C, respectively, then increases to 765.2 mAh g^{-1} when discharge rate returns to 0.1 C. As for the bare CuO, after ten cycles at a rate of 0.1 C, the discharge capacity is 637.3 mAh g^{-1}, and this decreases fast with increasing rate. Even when discharge rate recovers to 0.1 C, the discharge specific capacity still maintains 587.0 mAh g^{-1}, but it decreases fast to 250.8 mAh g^{-1} after 20 cycles, which may be because low conductivity of CuO and slow Li-ion diffusion lead to serious electrode pulverization.[42] Electrochemical impedance spectroscopy (EIS) of the prepared CuO samples after 20 cycles at 0.1 C are analyzed to deeply understand their Li-storage performance. The Nyquist plots and equivalent circuit are shown in Fig. 8c, which are composed of an intercept related to the internal resistance of the cell (R_e), two sequential semicircles at high-to-medium frequency separately corresponding to film impedance (R_{sf}//CPE_{sf}),

charge-transfer impedance (R_{ct}//CPE_{dl}), and a slope line corresponding to Warburg impedance (W_o) over Li^+ diffusion in solid materials.[32, 43] Thus, the semicircle appeared in the high-medium frequency range is attributed to the charge-transfer resistance occurring between active materials and liquid electrolyte, and the straight line is assigned to the Li-ion diffusion within electrode.[28, 39] It clearly shows the diameter of the semicircle for CuO/GO hybrid is much smaller than that of the bare CuO MSs, indicating a lower charge-transfer resistance and more facile electronic transportation. Therefore, the incorporation of GO significantly decreases the charge-transfer resistance and enhances electrochemical kinetics of the CuO/GO hybrid electrode.

Here, the improved electrochemical performance of the CuO/GO hybrid is attributed to the outstanding properties of GO and the porous hierarchical structures of CuO MSs. First, porous hierarchical structures of CuO can not only increase the surface area of the active materials but also mitigate the volume changes during the charge/discharge processes. Next, CuO wrapped by high conductive and flexible GO sheets endows the composites with good conductivity and high stability. Namely, GO sheets hybridized with CuO not only facilitate effective charge-transport and Li-ion diffusion, but also reduce the strain caused by volume variation and hinder the agglomeration of CuO particles over repeated discharge/charge cycles. Therefore, GO encapsulated porous hierarchical structures of CuO composites offer a promising alternative electrode material for high-performance LIB.

4. Conclusions

In summary, we have developed a facile, surfacant-free, carbonate-assisted hydrothermal method for synthesis of porous hierarchical CuO MSs and then through solution ionic strength engineering CuO Mss are successfully wrapped up by GO. By integrating superior properties of GO with unique CuO microstructures, we significantly improve the conductivity, mechanical flexiblility and stability of the CuO/GO composites. When used as promising anode materials for LIBs, the CuO/GO composites exhibit much higher lithium-storage capacities, better cycling durability and rate performance compared to bare CuO MSs. The CuO/GO hybrid eletrodes can deliver an initial capacity of 912.8 mAh g^{-1} at a rate of 0.5 C and retain a high reversible capacity of 500.0 mAh g^{-1} after 500 cycles, with 80% retention of the second reversible capacity. This work not only proposes a facile hydrothermal method for synthesis of porous hierarchical CuO, but also confirms an effective strategy for fabricating of potential high-performance LIB anodes by coating GO sheets on unique MO structures.

Acknowledgements

RSC Advances Accepted Manuscript

ARTICLE

Notes and references

1   M. Armand and J. M. Tarascon, *Nature*, 2008, 451, 652.
2   J. B. Dunn, L. Gaines, J. C. Kelly, C. James and K. G. Gallagher, *Energy Environ. Sci.*, 2015, 8, 158.
3   J. Liu, J. G. Zhang, Z. G. Yang, J. P. Lemmon, C. Imhoff, G. L. Graff, L. Y. Li, J. Z. Hu, C. M. Wang, J. Xiao, G. Xia, V. V. Viswanathan, S. Baskaran, V. Sprenkle, X. L. Li, Y. Y. Shao and B. Schwenzer, *Adv. Funct. Mater.*, 2013, 23, 929.
4   M. M. Thackeray, C. Wolverton and E. D. Isaacs, *Environ. Sci.*, 2012, 5, 7854.
5   J. B. Goodenough, *Energy Environ. Sci.*, 2014, 7, 14.
6   X. H. Xia, Y. Q. Zhang, D. L. Chao, C. Guan, Y. J. Zhang, L. Li, X. Ge, I. M. Bacho, J. P. Tu and H. J. Fan, *Nanoscale*, 2014, 6, 5008.
7   M. Osiak, H. Geaney, E. Armstrong and C. O'Dwyer, *J. Mater. A*, 2014, 2, 9433.
8   M. V. Reddy, G. V. Subba Rao and B. V. R. Chowdari, *Chem. Rev.* 2013, 113, 5364.
9   Y. Wang, Z. S. Feng, C. Zhang, L. Yu, J. J. Chen, J. Hu and X. Z. Liu, *Nanoscale*, 2013, 5, 3704.
10 Y. Wang, Z. S. Feng, L. L. Wang, L. Yu. J. J. Chen, Z, Liang and R. Wang, *RSC Adv.*, 2014, 4, 51609.
11 P. Poizot, S. Laruelle, S. Grugeon, L. Dupont and J. M. Tarascon, *Nature*, 2000, 407, 496.
12 L. Zhang, H. B. Wu and X. W. Lou, *Adv. Energy Mater.*, 2013, 4, 1300958.
13 X. Y. Qin, H. R. Zhang, J. X. Wu, X. D. Chu, Yan. B. He, C. P. Han, C. Miao, S. Wang, B. H. Li and F. Y. Kang, *Carbon*, 2015, 87, 347.
14 D. H. Ge, H. B. Geng, J. Q. Wang, J. W. Zheng, Y. Pan, X. Q. Cao and H. W. Gu, *Nanoscale*, 2014, 6, 9689.
15 G. Huang, F. F. Zhang, X. C. Du, Y. L. Qin, D. M. Yin and L. M. Wang, *ACS NANO*, 2015, 9, 1592.
16 H. L. Wang, L. F. Cui, Y. Yang, H. S. Casalongue, J. T. Robinson, Y. Y. Liang, Y. Cui and H. J. Dai, *J. Am. Chem. Soc.*, 2010, 132, 13978.
17 S. Z. Huang, Y. Cai, J. Jin, J. Liu, Y. Li, Y. Yu, H. E. Wang, L. H. Chen and B. L. Su, *Nano Energy*, 2015, 12, 833.
18 W. X. Zhang, M. Li, Q. Wang, G. D. Chen, M. Kong, Z. H. Yang and S. Mann, *Adv. Funct. Mater.*, 2011, 21, 3516.
19 S. Ko, J. I. Lee, H. S. Yang, S. Park and U. Jeong, *Adv. Mater.*, 2012, 24, 4451.
20 Q. B. Zhang, K. L. Zhang, D. G. Xu, G. C. Yang, H. Huang, F. D. Nie, C. M. Liu and S. H. Yang, *Prog. Mater. Sci.*, 2014, 60, 208.
21 D. Deng and J. Y. Lee, *ACS Appl. Mater. Interfaces*, 2014, 6, 1173.
22 L. Shi, C. Y. Fan, C. X. Sun, Z. M. Ren, X. X. Fu, G. D. Qian and Z. Y. Wang, *RSC Adv.*, 2015, 5, 28611.
23 Y. Zhang, M. W. Xu, F. Wang, X. P. Song, Y. H. Wang and S. Yang, *J. Phys. Chem. C*, 2013, 117, 12346.
24 H. W. Huang, Y. Liu, J. H. Wang, M. X. Gao, X. S. Peng and Z. Z. Ye, *Nanoscale*, 2013, 5, 1785.
25 S. F. Zheng, J. S. Hu, L. S. Zhong, W. G. Song, L. J. Wan, and Y. G. Guo, *Chem. Mater.*, 2008, 20, 3617.
26 C. R. Zhu, D. L. Chao, J. Sun, I. M. Bacho, Z. X. Fan, C. F. Ng, X. H. Xia, H. Huang, H. Zhang, Z. X. Shen, G. Q. Ding and H. J. Fan, *Adv. Mater. Interfaces*, 2015, 2, 1400499.
27 J. W. Ko, S. W. Kim, J. Hong, J. Ryu, K. Kang and C. B. Park, *Green Chem.*, 2012, 14, 2391.
28 Y. Liu, W. Wang, L. Gu, Y. W. Wang, Y. L. Ying, Y. Y. Mao, L. W. Sun and X. S. Peng, *ACS Appl. Mater. Interfaces*, 2013, 5, 9850.
29 Z. G. Yin, W. B. Fan, Y. H. Ding, J. X. Li, L. H. Guan and Q. D. Zheng, *ACS Sustainable Chem. Eng.*, 2015, 3, 507.
30 J. P. Rong, M. Y. Ge, X. Fang and C. W. Zhou, *Nano Lett.*, 2014, 14, 473-479.
31 Y. Liu, Y. L. Ying, Y. Y. Mao, L. Gu, Y. W. Wang and X. S. Peng, *Nanoscale*, 2013, 5, 9134.
32 W. X. Zhang, Z. Y. Zhou, W. R. Zhao, Z. H. Yang and X. N. Yang, *J. Mater. Chem. A*, 2014, 2, 5800.
33 A. Débart, L. Dupont, P. Poizot, J-B Leriche and J. M. Tarascon, *J. Electrochem. Soc.*, 2001, 148, A1266.
34 J. Y. Xiang, J. P. Tu, Y. Q. Qiao, X. L. Wang, J. Zhong, D. Zhang and C. D. Gu, *J. Phys. Chem. C*, 2011, 115, 2205.
35 Z. Y. Wang, F. B. Su, S. Madhavi, and X. W. Lou, *Nanoscale*, 2011, 3, 1618.
36 X. Wang, D. M. Tang, H. Q. Li, W. Yi, T. Y. Zhai, Y. Bando and D. Golberg, *Chem. Commun.*, 2012, 48, 4812.
37 X. Chen, N. Q. Zhang and K. N. Sun, *J. Phys. Chem. C*, 2012, 116, 21224.
38 R. Sahay, P. Suresh Kumar, V. Aravindan, J. Sundaramurthy, W. Chui Ling, S. G. Mhaisalkar, S. Ramakrishna and S. Madhavi, *J. Phys. Chem. C*, 2012, **116**, 18087.
39 C. Wang, Q. Li, F. F. Wang, G. F. Xia, R. Q. Liu, D. Y. Li, N. Li, J. S. Spendelow and G. Wu, *ACS Appl. Mater. Interfaces*, 2014, 6, 1243.
40 S. Laruelle, S. Grugeon, P. Poizot, M. Dollé, L. Dupont and J. M. Tarascon, *J. Electrochem. Soc.*, 2002, 149, A627.
41 K. M. Shaju, F. Jiao, A. Débart and P. G. Bruce, *Phys. Chem. Chem. Phys.*, 2007, 9, 1837.
42 L. Q. Lu and Y. Wang, *Electrochem. Commun.,* 2012, 14, 82.
43 Q. B. Zhang, J. X. Wang, D. G. Xu, Z. X. Wang, X. H. Li and K. L. Zhang, *J. Mater. Chem. A*, 2014, 2, 3865.